

Towards Robustness against Unsuspicious Adversarial Examples

Liang Tong¹ Minzhe Guo¹ Atul Prakash² Yevgeniy Vorobeychik¹

Abstract

Despite the remarkable success of deep neural networks, significant concerns have emerged about their robustness to adversarial perturbations to inputs. While most attacks aim to ensure that these are imperceptible, *physical* perturbation attacks typically aim for being unsuspicious, even if perceptible. However, there is no universal notion of what it means for adversarial examples to be unsuspicious. We propose an approach for modeling suspiciousness by leveraging cognitive salience. Specifically, we split an image into foreground (salient region) and background (the rest), and allow significantly larger adversarial perturbations in the background. We describe how to compute the resulting dual-perturbation attacks on both deterministic and stochastic classifiers. We then experimentally demonstrate that our attacks do not significantly change perceptual salience of the background, but are highly effective against classifiers robust to conventional attacks. Furthermore, we show that adversarial training with dual-perturbation attacks yields classifiers that are more robust to these than state-of-the-art robust learning approaches, and comparable in terms of robustness to conventional attacks.

1. Introduction

An observation by Szegedy et al. (2014) that state-of-the-art deep neural networks that exhibit exceptional performance in image classification are fragile in the face of small adversarial perturbations of inputs has received a great deal of attention. A series of approaches for designing adversarial examples followed (Szegedy et al., 2014; Goodfellow et al., 2015; Carlini & Wagner, 2017), along with methods for defending against them (Papernot et al., 2016b; Madry et al., 2018), and then new attacks that defeat prior defenses, and so on. Attacks can be roughly classified along three dimensions: 1) introducing small l_p -norm-bounded perturbations,

¹Washington University in St. Louis ²University of Michigan. Correspondence to: Liang Tong <liangtong@wustl.edu>.

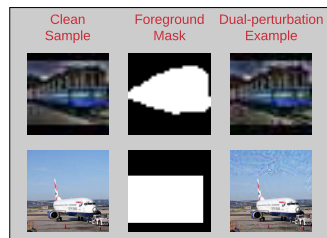


Figure 1. An illustration of dual-perturbation attacks. The top uses semantic segmentation to identify foreground and background. The bottom uses object bounding box.

with the goal of these being imperceptible to humans (Madry et al., 2018), 2) using non- l_p -based constraints that capture perceptibility (often called *semantic perturbations*) (Bhattad et al., 2020), and 3) modifying physical objects, such as stop signs (Eykholt et al., 2018), in a way that does not arouse suspicion. One of the most common motivations for the study of adversarial examples is safety and security, such as the potential for attackers to compromise the safety of autonomous vehicles that rely on computer vision (Eykholt et al., 2018). However, while imperceptibility is certainly sufficient for perturbations to be unsuspicious, it is far from necessary, as physical attacks demonstrate. On the other hand, while there are numerous formal definitions that capture whether noise is perceptible (Moosavi-Dezfooli et al., 2016; Carlini & Wagner, 2017), what makes adversarial examples suspicious has been largely informal and subjective.

We propose a simple formalization of an important aspect of what makes adversarial perturbations unsuspicious. Specifically, we make a distinction between image foreground and background, allowing significantly more noise in the background than the foreground. This idea stems from the notion of cognitive salience (Borji et al., 2015; Kmmmerer et al., 2017; He & Pugeault, 2018), whereby an image can be partitioned into the two respective regions to reflect how much attention a human viewer pays to the different parts of the captured scene. In effect, we posit that perturbations in the foreground, when visible, will arouse significantly more suspicion (by being cognitively more salient) than perturbations made in the background.

Our first contribution is a formal model of such *dual-*

perturbation attacks, which is a generalization of the ℓ_p -norm-bounded attack models. Second, we propose an algorithm for finding adversarial examples using this model, which is an adaptation of the PGD attack (Madry et al., 2018), as well as two approaches for partitioning images into foreground and background, the first using object detection and the second using segmentation (see, e.g., Figure 1). Third, we present two methods for defending against dual-perturbation attacks, both based on the adversarial training framework (Madry et al., 2018). Finally, we present an extensive experimental study that demonstrates that (a) the proposed attacks are significantly stronger than PGD, successfully defeating all state-of-the-art defenses, (b) proposed defenses using our attack model significantly outperform state-of-the-art alternatives, *with relatively small performance degradation on non-adversarial instances*, and (c) proposed defenses are comparable to, or better than alternatives *even against traditional attacks*, such as PGD.

Related Work Recent studies have shown that neural networks are vulnerable to adversarial examples. A variety of approaches have been proposed to produce adversarial examples (Szegedy et al., 2014; Goodfellow et al., 2015; Papernot et al., 2016a; Moosavi-Dezfooli et al., 2016; Carlini & Wagner, 2017). These approaches commonly generate adversarial perturbations within a bounded ℓ_p norm so that the perturbations are imperceptible. A related thread has considered the problem of generating adversarial examples that are semantically imperceptible without being small in norm (Brown et al., 2018; Bhattad et al., 2020), for example, through small perturbations to the color scheme. However, none of these account for the perceptual distinction between the foreground and background of images.

Numerous approaches have been proposed for defending neural networks against adversarial examples (Papernot et al., 2016b; Carlini & Wagner, 2017; Madry et al., 2018; Cohen et al., 2019; Madry et al., 2018; Raghunathan et al., 2018). Predominantly, these use ℓ_p -bounded perturbations as the threat model, and while some account for semantic perturbations (e.g. (Mohapatra et al., 2020)), none consider perceptually important difference in suspiciousness between foreground and background.

A recent approach by Vaishnavi et al. (2019) has the strongest conceptual connection to our work. However, it is defense-focused, and *assumes* that we can reliably segment an image *at prediction time*, leaving the approach vulnerable to attacks on image segmentation (Arnab et al., 2018).

2. Background

In this section, we first introduce adversarial examples and attacks to produce these. We then summarize two representative approaches for training neural networks that are

robust to adversarial examples.

2.1. Adversarial Examples and Attacks

The problem of generating adversarial examples is commonly modeled as follows. We are given a learned model $h_\theta(\cdot)$ parameterized by θ which maps an input x to a k -dimensional prediction, where k is the number of classes being predicted. The final predicted class y_p is obtained by $y_p = \arg \max_i h_\theta(x)_i$, where $h_\theta(x)_i$ is the i th element of $h_\theta(x)$. Now, consider an input x along with a correct label y . The problem of identifying an adversarial example for x can be captured by the following optimization problem:

$$\max_{\delta \in \Delta(\epsilon)} \mathcal{L}(h_\theta(x + \delta), y) \quad (1)$$

where $\mathcal{L}(\cdot)$ is the loss function used to train the classifier h_θ and $\Delta(\epsilon)$ is the feasible perturbation space which is commonly represented as a ℓ_p ball: $\Delta(\epsilon) = \{\delta : \|\delta\|_p \leq \epsilon\}$.

A number of approaches have been proposed to solve the optimization problem shown in Eq. (1), among which two are viewed as state of the art: *CW attack* developed by (Carlini & Wagner, 2017), and *Projected Gradient Descent (PGD) attack* proposed in Madry et al. (2018). In this work, we focus on the PGD attack with ℓ_∞ and ℓ_2 as the distance metrics. In the PGD approach, we solve the problem in Eq. (1) by iteratively updating the adversarial perturbation as follows:

$$\delta^{(k+1)} = \mathcal{P}_\epsilon(\delta^{(k)} + \alpha \mathcal{G}(\nabla_{\delta^{(k)}} \mathcal{L}(h_\theta(x + \delta^{(k)}), y))) \quad (2)$$

where $\delta^{(k)}$ is the perturbation at the k -th iteration, α is the step size in each iteration, \mathcal{P}_ϵ is a projection to ensure that $\delta^{(k)}$ is feasible, for example, $\|\delta\|_p \leq \epsilon$ and $x + \delta^{(k)}$ is clipped to feasible pixel values; and \mathcal{G} returns the update corresponding to the *normalized steepest descent* given the gradient. Note that both the realization of \mathcal{P}_ϵ and \mathcal{G} depend on the ℓ_p distance used in the PGD attack. Specifically, for the ℓ_∞ PGD attack,

$$\begin{cases} \mathcal{G}(m) = \text{sign}(m) \\ \mathcal{P}_\epsilon(n) = \text{clip}(n, [-\epsilon \mathbf{1}, +\epsilon \mathbf{1}] \cap [-x, \mathbf{1} - x]) \end{cases}$$

where sign returns the sign matrix of an input, $\mathbf{1}^1$ is an all-ones matrix that has the same dimensions as $\delta^{(k)}$, and clip is an operator that clip the each element of a given input in an element-wise manner. When it comes to the ℓ_2 PGD attack,

$$\begin{cases} \mathcal{G}(m) = \frac{m}{\|m\|_2} \\ \mathcal{P}_\epsilon(n) = \text{clip}(\frac{\epsilon n}{\max\{\epsilon, \|n\|_2\}}, [-x, \mathbf{1} - x]) \end{cases}$$

¹Generally, images are preprocessed such that pixels are divided by 255 for computational convenience in training and testing. Consequently, a feasible pixel value should lie in $[0, 1]$.

Since the adversarial optimization problem is non-convex, PGD is typically augmented by using a number of random starting points for adversarial perturbations that are close to the original input \mathbf{x} (Madry et al., 2018).

2.2. Robust Learning

Here, we describe two categorizations of defense that have proved both sufficiently scalable and effective even against adaptive attacks: *adversarial training* (Szegedy et al., 2014; Cohen et al., 2019; Goodfellow et al., 2015; Madry et al., 2018) and *randomized smoothing* (Cohen et al., 2019; Lecuyer et al., 2019).

Adversarial Training. The basic idea of adversarial training is to produce adversarial examples and incorporate these into the training process. Formally, adversarial training aims to solve the following robust learning problem:

$$\min_{\theta} \frac{1}{|D|} \sum_{\mathbf{x}, y \in D} \max_{\|\delta\|_p \leq \epsilon} \mathcal{L}(h_{\theta}(\mathbf{x} + \delta), y) \quad (3)$$

where D is the training dataset. In practice, this problem is commonly solved by iteratively using the following two steps (Madry et al., 2018): 1) use a PGD (or other) attack to produce adversarial examples of the training data; 2) use any optimizer to minimize the loss of those adversarial examples. It has been shown that adversarial training can significantly boost the adversarial robustness of a classifier against ℓ_p attacks, and it can be scaled to neural networks with complex architectures.

Randomized Smoothing. The second class of methods for robust learning considers adding random perturbations to inputs at both training and test time. The basic idea is to construct a new smoothed classifier $g_{\theta}(\cdot)$ from a base classifier $h_{\theta}(\cdot)$ as follows: first, the base classifier $h_{\theta}(\cdot)$ is trained with *Gaussian data augmentation* with variance σ^2 ; then, for any input \mathbf{x} at test time, the smoothed classifier $g_{\theta}(\cdot)$ returns the class that has the highest probability measure for the base classifier $h_{\theta}(\cdot)$ when inputs are perturbed with isotropic Gaussian noise:

$$g_{\theta}(\mathbf{x}) = \arg \max_c P(h_{\theta}(\mathbf{x} + \boldsymbol{\eta}) = c) \quad (4)$$

where $\boldsymbol{\eta} \sim \mathcal{N}(\mathbf{0}, \sigma^2 \mathbf{I})$

It has been shown that randomized smoothing can provide *certified robustness* to adversarial perturbations for ℓ_2 -norm-bounded attacks (Cohen et al., 2019; Lecuyer et al., 2019).

3. Dual-Perturbation Attacks

In this section, we introduce a novel threat model, the *dual-perturbation attack*, against state-of-the-art adversarially robust image classification models. Below, we first describe the motivation of the proposed attack. Then, we turn to technical details.



Figure 2. Semantic distinction between foreground and background. Left: Original image of a train. Middle: Adversarial example with ℓ_{∞} bounded perturbations ($\epsilon = 60/255$) on the background, the semantic meaning (train) is preserved. Right: Adversarial example with ℓ_{∞} bounded perturbations ($\epsilon = 60/255$) on the foreground, the semantics are broken.

3.1. Motivation

Our threat model is motivated by the *feature integration theory* (Treisman & Gelade, 1980) in cognitive science: regions that have features that are different from their surroundings are more likely to catch a viewer’s gaze. Such regions are called *salient regions*, or *foreground*, while the others are called *background*. Accordingly, for a given image, the semantics of the object of interest is more likely to be preserved in the foreground, as it catches more visual attention of a viewer compared to the background. If the foreground of an image is corrupted, then the semantics of the object of interest is broken. In contrast, the same extent of corruption in the background nevertheless preserves the overall semantic meaning of the scene captured (see, e.g., Figure 2). Indeed, detection of salient regions, as well as the segmentation of foreground and background, have been extensively studied in computer vision (Borji et al., 2015). These approaches either predict human fixations, which are sparse bubble-like salient regions sampled from a distribution (Kimmerer et al., 2017), or salient objects that contain smooth connected areas in an image (He & Pugeault, 2018).

Despite this important cognitive distinction between foreground and background, essentially all of the attacks on deep neural networks for image classification make no such distinction, even though a number of other semantic factors have been considered (Bhattad et al., 2020; Mohapatra et al., 2020). Rather, much of the focus has been on adversarial perturbations that are *not noticeable* to a human, but which are applied *equally to the entire image*. However, in security applications, the important issue is not merely that an attack cannot be noticed, but that whatever is observed is *not suspicious*. This is, indeed, the frame of reference for many high-profile *physical* attacks on image classification, which are clearly visible, but not suspicious because they hide in the “human psyche”, that is, are easily ignored (Sharif et al., 2016; Eykholt et al., 2018). The main goal of the threat model we introduce next is therefore to capture more precisely the notion that an adversarial example is not suspicious by leveraging the cognitive distinction

between foreground and background of an image.

3.2. Dual-Perturbation Attacks

At the high level, our proposed threat model involves producing small (imperceptible) adversarial perturbations in the foreground of an image, and larger perturbations in the background. This can be done by incorporating state-of-the-art attacks into our method: we can use one attack with small ϵ in the foreground, and another with a large ϵ in the background. Consequently, we term our approach *dual-perturbation attacks*. Note that these clearly generalize the standard small-norm (e.g., PGD) attacks, since we can set the ϵ to be identical in both the foreground and background.

Formally, the *dual-perturbation* attack solves the following optimization problem:

$$\max_{\|\delta \circ \mathcal{F}(\mathbf{x})\|_p \leq \epsilon_F, \|\delta \circ \mathcal{B}(\mathbf{x})\|_p \leq \epsilon_B} \mathcal{L}(h_\theta(\mathbf{x} + \delta), y) \quad (5)$$

where \mathcal{F} returns the mask matrix constraining the area of the perturbation in the foreground, and \mathcal{B} returns the mask matrix restricting the area of the perturbation in the background, for an input image \mathbf{x} . $\mathcal{F}(\mathbf{x})$ and $\mathcal{B}(\mathbf{x})$ have the same dimension as \mathbf{x} and contain 1s in the area which can be perturbed and 0s elsewhere. \circ denotes element-wise multiplication for matrices. Hence, we have $\mathbf{x} = \mathcal{F}(\mathbf{x}) + \mathcal{B}(\mathbf{x})$ which indicates that any input image can be decomposed into two independent images: one containing just the foreground, and the other containing the background.

A natural approach for solving the optimization problem shown in Eq.(5) is to apply an iterative method, such as the PGD attack, as shown in (2). However, the use of this approach poses two challenges in our setting. First, as in the PGD attack, the problem is non-convex, and PGD only converges to a local optimum. We can address this issue by using *random starts*, i.e. by randomly initializing the starting point of the adversarial perturbations, as in Madry et al. (2018). Second, and unlike PGD, the optimization problem in Eq.(5) involves *two hard constraints* $\|\delta \circ \mathcal{F}(\mathbf{x})\|_p \leq \epsilon_F$ and $\|\delta \circ \mathcal{B}(\mathbf{x})\|_p \leq \epsilon_B$. Thus, the feasible region of the adversarial perturbation δ is not an ℓ_p ball, which makes computing the projection \mathcal{P}_ϵ computationally challenging in high-dimensional settings. To address this challenge, we split the *dual-perturbation* attack into two individual processes in each iteration, one for the adversarial perturbation in the foreground and the other for the background, and then merge these two perturbations when computing the gradients, like a standard PGD attack. Specifically, we use the following steps to solve the optimization problem in Eq.(5):

1. *Initialization*. Start with a random initial starting point $\delta^{(0)}$. To do this, randomly sample a data point $\delta_F^{(0)}$ in ℓ_p ball $\Delta(\epsilon_F)$ and $\delta_B^{(0)}$ in $\Delta(\epsilon_B)$. Then, $\delta^{(0)}$ can be

obtained by using $\delta^{(0)} = \delta_F^{(0)} \circ \mathcal{F}(\mathbf{x}) + \delta_B^{(0)} \circ \mathcal{B}(\mathbf{x})$. This ensures that the initial perturbation is feasible in both foreground and background.

2. *Split*. At the k -th iteration, split the perturbation $\delta^{(k)}$ into $\delta_F^{(k)}$ for foreground and $\delta_B^{(k)}$ for background:

$$\begin{cases} \delta_F^{(k)} = \delta^{(k)} \circ \mathcal{F}(\mathbf{x}) \\ \delta_B^{(k)} = \delta^{(k)} \circ \mathcal{B}(\mathbf{x}) \end{cases} \quad (6)$$

Then update the foreground and background perturbations separately using the following rules:

$$\begin{cases} \delta_F^{(k+1)} = \mathcal{P}_\epsilon(\delta_F^{(k)} + \alpha_F \cdot g_F) \\ \delta_B^{(k+1)} = \mathcal{P}_\epsilon(\delta_B^{(k)} + \alpha_B \cdot g_B) \end{cases} \quad (7)$$

where g_F is the update that corresponds to the *normalized steepest descent* constrained in the foreground, and g_B for the background. Specifically,

$$\begin{cases} g_F = \mathcal{G}(\mathcal{F}(\mathbf{x}) \circ \nabla_{\delta^{(k)}} \mathcal{L}(h_\theta(\mathbf{x} + \delta^{(k)}), y)) \\ g_B = \mathcal{G}(\mathcal{B}(\mathbf{x}) \circ \nabla_{\delta^{(k)}} \mathcal{L}(h_\theta(\mathbf{x} + \delta^{(k)}), y)) \end{cases} \quad (8)$$

where α_F is the stepsize for foreground, and α_B is the stepsize for background.

3. *Merge*. At the end of the k -th iteration, merge the perturbations obtained in the last step by using

$$\delta^{(k+1)} = \delta_F^{(k+1)} + \delta_B^{(k+1)}. \quad (9)$$

$\delta^{(k+1)}$ is further used to derive the update for the normalized steepest descent at the next iteration.

4. Return to step 2 or terminate after either a fixed number of iterations.

In addition to *deterministic classifiers* that make a deterministic prediction for a test sample, our proposed attack can be adapted to *stochastic classifiers* that apply randomization at training and prediction time. For example, for classifiers using *randomized smoothing*, we can refine Eq.(5) as follows:

$$\max_{\|\delta \circ \mathcal{F}(\mathbf{x})\|_p \leq \epsilon_F, \|\delta \circ \mathcal{B}(\mathbf{x})\|_p \leq \epsilon_B} \mathbb{E}_{\boldsymbol{\eta} \sim \mathcal{N}(\mathbf{0}, \sigma^2 I)} [\mathcal{L}(h_\theta(\mathbf{x} + \delta + \boldsymbol{\eta}), y)] \quad (10)$$

where σ^2 is the variance of the Gaussian data augmentation in randomized smoothing.² The optimization problem in Eq.(10) can be solved by the same approach used for deterministic classifiers, with the following modification on

²Note that the Gaussian perturbations are only used to compute the expectation of loss and are not in the resulting adversarial examples.

Eq.(8) at the second step:

$$\begin{cases} g_F = \mathcal{G}(\mathcal{F}(\mathbf{x}) \circ \nabla_{\delta^{(k)}} \mathbb{E}_{\eta}[\mathcal{L}(h_{\theta}(\mathbf{x} + \delta^{(k)} + \eta), y)]) \\ g_B = \mathcal{G}(\mathcal{B}(\mathbf{x}) \circ \nabla_{\delta^{(k)}} \mathbb{E}_{\eta}[\mathcal{L}(h_{\theta}(\mathbf{x} + \delta^{(k)} + \eta), y)]) \end{cases} \quad (11)$$

Now, the question that remains is how to partition an input image \mathbf{x} into foreground, $\mathcal{F}(\mathbf{x})$, and background, $\mathcal{B}(\mathbf{x})$. We address this next.

3.3. Identifying Foreground and Background

We now turn to our approach to compute the foreground and background masks for an input image: Given an input \mathbf{x} , we aim to compute $\mathcal{F}(\mathbf{x})$, the foreground mask and $\mathcal{B}(\mathbf{x})$, the background mask. We use two approaches for this: object detection and segmentation.

Our first approach leverages the object detection approaches (Redmon & Farhadi, 2018) to obtain the bounding box of the object of interest as the foreground. A bounding box is a rectangular box that can be determined by the axis coordinates in the upper-left corner, and the axis coordinates in the lower-right corner of the rectangle. Once we obtained all the bounding boxes of a given image, we can filter out those that are irrelevant to the object of interest and combine the remaining boxes such that the area inside the union of the boxes is identified as foreground, and the area outside is identified as background.

Our second approach is to make use of semantic segmentation to provide a partition of the foreground and background in pixel level. This can be done in two steps: First, we use state-of-the-art paradigms for semantic segmentation (e.g., Long et al. (2015)) to identify pixels that belong to each corresponding object, as there might be multiple objects in an image. Next, we identify the pixels that belong to the object of interest as the foreground pixels, and the others as background pixels.

We use both of the above approaches in dual-perturbation attacks when evaluating the robustness of classifiers, as well as designing robust models. More details are available in Section 5.

4. Defense against Dual-Perturbation Attacks

Once we are able to compute the dual-perturbation attack, we can incorporate it into conventional adversarial training paradigms for defense, as it has been demonstrated that adversarial training is highly effective in designing classification models that are robust to a given attack. Specifically, we propose two defense approaches that we describe next.

Adversarial Training with dual-perturbation. We replace the PGD attack in the adversarial training framework proposed by Madry et al. (2018), with the proposed dual-

perturbation attack. We term this approach *AT-Dual*, which aims to solve the following optimization problem:

$$\min_{\theta} \frac{1}{|D|} \sum_{\mathbf{x}, y \in D} \max_{\substack{\|\delta \circ \mathcal{F}(\mathbf{x})\|_p \leq \epsilon_F, \\ \|\delta \circ \mathcal{B}(\mathbf{x})\|_p \leq \epsilon_B}} \mathcal{L}(h_{\theta}(\mathbf{x} + \delta), y) \quad (12)$$

MixTrain with dual-perturbation. As pointed out by Wang et al. (2018), conventional adversarial training can at times fail to converge for very strong attacks, and often significantly degrades clean data accuracy. To address these concerns, we incorporate dual-perturbation attack with MixTrain (Wang et al., 2018), a variant of adversarial training. The resulting approach, *Mix-Dual*, is formulated as follows:

$$\min_{\theta} \frac{1}{|D|} \sum_{\mathbf{x}, y \in D} \max_{\substack{\|\delta \circ \mathcal{F}(\mathbf{x})\|_p \leq \epsilon_F, \\ \|\delta \circ \mathcal{B}(\mathbf{x})\|_p \leq \epsilon_B}} \beta \mathcal{L}_1 + (1 - \beta) \mathcal{L}_2 \quad (13)$$

where \mathcal{L}_1 is the loss on adversarial examples such that

$$\mathcal{L}_1 = \mathcal{L}(h_{\theta}(\mathbf{x} + \delta), y),$$

and \mathcal{L}_2 is the loss on clean examples.

$$\mathcal{L}_2 = \mathcal{L}(h_{\theta}(\mathbf{x}), y).$$

$\beta \in [0, 1]$ is a parameter that trades off between \mathcal{L}_1 and \mathcal{L}_2 .

Note that both *AT-Dual* and *Mix-Dual* need to apply *object detection* method to identify background and foreground for any input when solving the inner maximization problems in Eq.(12) and Eq.(13) at training time. At prediction time, our approaches classify test samples like any standard classifiers, which is independent of the semantic partitions so as to close the backdoors to attacks on object detection approaches (Xie et al., 2017). We evaluate the effectiveness of our approaches in Section 5.

5. Experiments

In the section, we evaluate the effectiveness of the proposed dual-perturbation attack and defense approaches (*AT-Dual* and *Mix-Dual*).

5.1. Experimental Setup

Dataset	Image size	Training set size	Testing set size	Classes
Segment-6	$32 \times 32 \times 3$	18,000	1,200	6
STL-7	$96 \times 96 \times 3$	1,246	500	7
ImageNet-10	$224 \times 224 \times 3$	3,327	344	10

Table 1. Evaluation datasets.

Datasets. We conducted the experiments on the following three datasets, listed in Table 1. The first is Segment-6, obtained by pre-processing the Microsoft COCO dataset (Lin

et al., 2014) to make it compatible with image classification tasks. We used semantic segmentation to obtain the foreground masks on this dataset (see the Supplement for details). Our second dataset is STL-7, a subset of the STL-10 dataset (Coates et al., 2011). We chose this subset by filtering out those the objects of interest of which were not correctly detected by YOLOv3 (Redmon & Farhadi, 2018), the state-of-the-art object detection method. For each image in the dataset, we used YOLOv3 to identify the bounding box of the object of interest as the foreground. Our third dataset is ImageNet-10, a 10-class subset of the ImageNet dataset (Deng et al., 2009). We chose this subset of images and obtained the corresponding foreground masks by using the same approach as the STL-7 dataset.

Baselines. The performance of the proposed approach was compared with two alternative paradigms that have been proved to boost adversarial robustness: *Adversarial Training with PGD Attacks* (henceforth, *AT-PGD*) proposed in Madry et al. (2018), the state-of-the-art adversarially robust training scheme widely used in practice; *Randomized Smoothing* (henceforth, *RS*) in Cohen et al. (2019), which achieves provably robust classification against ℓ_2 attacks. Additionally, we compared our approach with the classifier trained on non-adversarial data (henceforth, *Clean*).

Evaluation Method. For a given classification model, we evaluated its performance in two ways: 1) Evaluated the accuracy of prediction on clean test data where no adversarial attacks were attempted. 2) Evaluated its adversarial robustness against different attacks by using the accuracy of prediction on corresponding adversarial examples.

Throughout our evaluation, we used both ℓ_2 and ℓ_∞ norms as the distance metrics to implement attacks, as well as the robust classification models that are based on adversarial training. The implementations of attacks and defense approaches are detailed in the Appendix. Due to space limitations, we only present experimental results of the *Clean* model and classification models that are trained to be robust to ℓ_2 norm attacks. The results for ℓ_∞ norm are similar and deferred to the Supplement.

5.2. Saliency Analysis of Dual-Perturbation Adversarial Examples

We begin by considering a natural question: is our particular distinction between foreground and background actually consistent with cognitive salience? In fact, this gives rise to two distinct considerations: 1) whether foreground as we identify it is in fact significantly more salient than the background, and 2) if so, whether background becomes significantly more salient as a result of our dual-perturbation attacks. We answer both of these questions by appealing to a recent computational model of image salience, DeepGaze

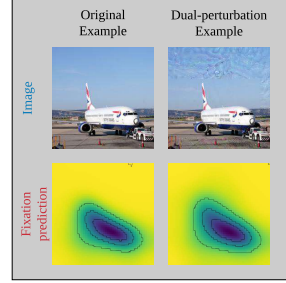


Figure 3. Examples of fixation prediction of a clean test example and adversarial example by using ℓ_2 dual-perturbation attack. The bottoms show fixation predictions of each example, where darker values represent higher probabilities of catching humans’ attention.

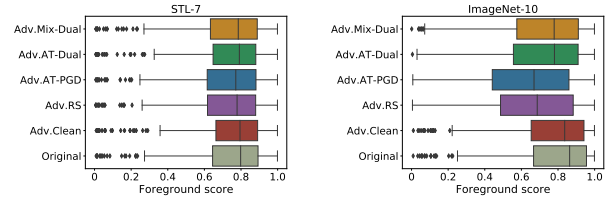


Figure 4. Saliency analysis: foreground score of the original and ℓ_2 dual-perturbation examples in response to different defense approaches. AT-PGD, AT-Dual, and Mix-Dual are trained by using ℓ_2 -norm attacks with hyper-parameters listed in Table 6 in the Supplement. RS uses $\sigma = 0.5$. Left: STL-7. The ℓ_2 dual-perturbation attack is performed with $\epsilon_F = 1$ and $\epsilon_B = 15$. Right: ImageNet-10. The ℓ_2 dual-perturbation attack is performed with $\epsilon_F = 2$ and $\epsilon_B = 30$.

II (Kimmerer et al., 2017).³ Concretely, DeepGaze II outputs predicted pixel-level density of human fixations on an image, as illustrated in Figure 3, with the total density over the entire image summing to 1. Our measure of relative salience of the foreground is the *foreground score* (*FS*), which is defined as $FS = \sum_{i \in \{k | \mathcal{F}(x)_k \neq 0\}} s_i$, where s_i is the saliency score produced by DeepGaze II for pixel i of image x . Since foreground, as a fraction of the image, tends to be around 50-60%, a score significantly higher than 0.5 indicates that predicted human fixation is relatively localized to the foreground.

Figure 4 presents the answer to both of the questions above, using *FS* as the metric. Specifically, we can see that *FS* tends to be close to 0.8 for STL-7, and above 0.8 for ImageNet-10, both for the original instances (addressing question 1) and for adversarial instances implemented against a non-robust deep neural network (addressing question 2). Moreover, we can see that this score does not statistically significantly de-

³Since DeepGaze II only work on images with more than 35×35 pixels, we conducted saliency analysis on STL-7 and ImageNet-10 for the purpose of demonstration.

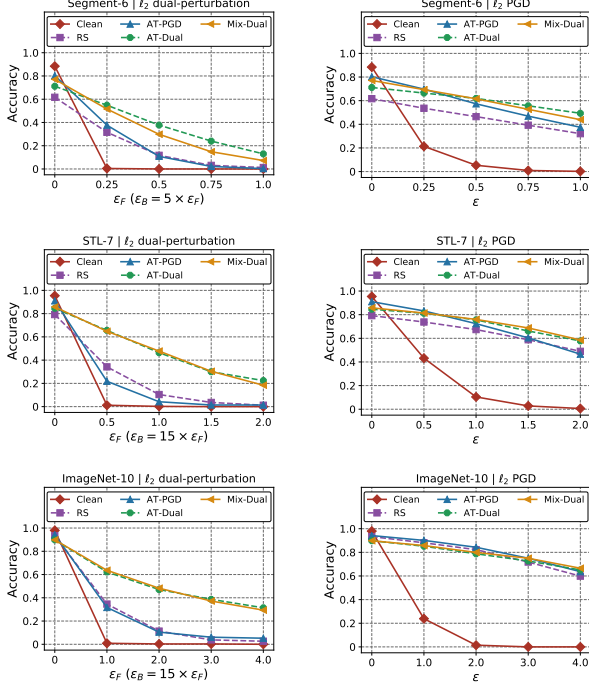


Figure 5. Robustness to white-box ℓ_2 attacks with a variety of distortions on Segment-6 (top row), STL-7 (middle row), and ImageNet-10 (bottom row). AT-PGD, AT-Dual and Mix-Dual are trained by using ℓ_2 -norm attacks with hyper-parameters listed in Table 6 in the Supplement. RS uses $\sigma = 0.5$. Left: dual-perturbation attacks. Right: PGD.

crease even when we attack robust classifiers. However, we do note some tangible decrease in the case of robust classifiers on ImageNet-10, suggesting another interesting dimension to the problem: it appears more difficult to generate unsuspicious adversarial examples against robust classifiers.

5.3. Dual-perturbation Attacks on Robust Classifiers

Next, we evaluate the effectiveness of dual-perturbation attacks against state-of-the-art robust learning methods, as well as the effectiveness of adversarial training variants that use dual-perturbation attacks for generating adversarial examples. We begin by considering white-box attacks, and subsequently evaluate transferability.

The results for white-box attacks are presented in Figure 5. First, consider the dual-perturbation attacks (left plots). Note that in all cases these attacks are highly successful against both baseline robust classifiers (AT-PGD and RS); indeed, even relatively small levels of foreground noise yield near-zero accuracy when accompanied by sufficiently large background perturbations. For example, when the perturbation to the foreground is $\epsilon_F = 1.0$ and background perturbation is $\epsilon_B = 15.0$ on STL-7 data, RS achieves robust

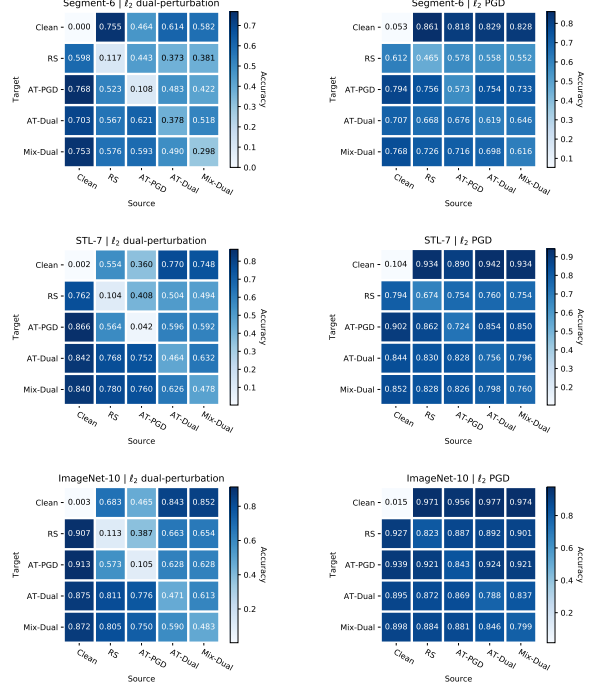


Figure 6. Transferability of adversarial examples on Segment-6 (top row), STL-7 (middle row), and ImageNet-10 (bottom row). AT-PGD, AT-Dual and Mix-Dual are trained by using corresponding ℓ_2 -norm attacks with hyper-parameters listed in Table 6 in the Supplement. RS uses $\sigma = 0.5$. Left: dual-perturbation attacks. Right: PGD.

accuracy below 10%, while AT-PGD only has 5% robust accuracy. In contrast, both of the defense approaches discussed, AT-Dual and Mix-Dual remain significantly more robust, with an improvement of up to 40% compared to the baselines, without sacrificing much in accuracy on clean data. Second, consider the standard PGD attacks (right plots). It can be observed that all of the robust models are successful against the ℓ_2 PGD attacks. However, in the cases of the Segment-6 and STL-7 datasets, our defenses exhibit moderately higher robustness than the baselines under large distortions of PGD attacks. For example, when the perturbation of the ℓ_2 PGD attack is $\epsilon = 2.0$ on the ImageNet-10 data, AT-Dual and Mix-Dual can achieve 10% more robust accuracy.

Next, we measure the *transferability* of adversarial examples among different classification models. To do this, we first produced adversarial examples by using ℓ_2 PGD attack or dual-perturbation attack on a source model. Then, we used these examples to evaluate the performance of an independent target model, where a higher prediction accuracy means weaker transferability. The results are presented in Figure 6. The first observation is that dual-perturbation attacks exhibit significantly better transferability than the

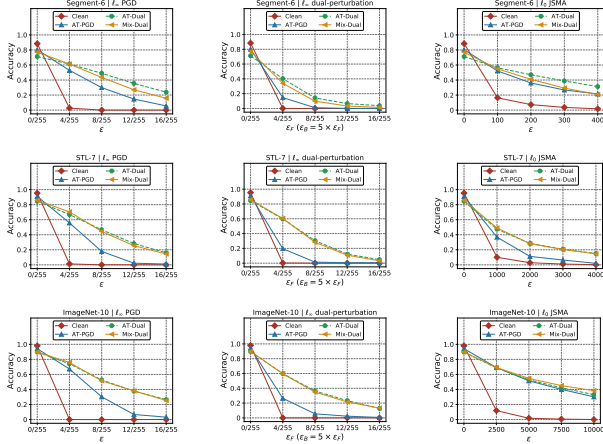


Figure 7. Robustness to additional white-box attacks on Segment-6 (top row), STL-7 (middle row), and ImageNet-10 (bottom row). AT-PGD, AT-Dual and Mix-Dual are trained by using corresponding l_2 -norm attacks with hyper-parameters listed in Table 6 in Appendix. Left: l_∞ PGD attacks. Middle: l_∞ dual-perturbation attacks. Right: l_0 JSMA attacks.

conventional PGD attacks (transferability is up to 40% better for dual-perturbation attacks). Second, we can observe that when either *AT-Dual* or *Mix-Dual* are used as the target (i.e., defending by adversarial training with dual-perturbation examples), these are typically resistant to adversarial examples generated against either the clean model, or against RS and *AT-PGD*. This observation obtains even when we use PGD to generate adversarial examples.

5.4. Generalizability of Defense

It has been observed that robustness against l_p -norm-bounded attacks for one value of p can be fragile when facing attacks with a different norm $l_{p'}$ (Sharma & Chen, 2018). Our final goal is to present evidence that the approaches for defense based on dual-perturbation attacks remain relatively robust even when faced with attacks generated using different norms. Here, we show this when our models are trained using the l_2 -bounded attacks, and evaluated against other attacks using other norms. Data for models trained using l_∞ -bounded attacks is provided in the Supplement.

The results are presented in Figure 7. We again present the results for three datasets: Segment-6 (where foreground is determined using segmentation), top row, STL-7, middle row, and ImageNet-10, bottom row. We consider three alternative attacks: 1) PGD using the l_∞ -bounded perturbations, as in Madry et al. (Madry et al., 2018) (left column in Figure 7) 2) dual-perturbation attacks with l_∞ -norm bounds (middle column in Figure 7), and 3) JSMA, a l_0 -bounded attack (Papernot et al., 2016a) (right column in Figure 7).

We additionally considered l_2 attacks, per Carlini and Wagner (Carlini & Wagner, 2017), but find that all of the robust models, whether based on PGD or dual-perturbation attacks, are successful against these.

Our first observation is that both *AT-Dual* and *Mix-Dual* are significantly more robust to l_∞ -bounded PGD attacks than the adversarial training approach in which adversarial examples are generated using l_2 -bounded PGD attacks. Moreover, the magnitude of the advantage appears to increase with more complex datasets: the gap is larger for STL-7 and ImageNet-10 compared to Segment-6. Consequently, training with dual-perturbation attacks already exhibits better ability to generalize to other attacks compared to conventional adversarial training.

The gap between dual-perturbation-based adversarial training and standard adversarial training is even more significant when we consider l_∞ dual-perturbation attacks (middle column). Here, we see that robustness of PGD-based adversarially trained model is only marginally better than that of a clean model, whereas both *AT-Dual* and *Mix-Dual* remain relatively robust.

Finally, considering JSMA attacks, we can observe that on two of the three datasets (Segment-6 and ImageNet), conventionally adversarially trained model remains relatively robust. However, STL-7 exhibits a case where this model is indeed fragile to l_0 -bounded attacks. In contrast, in all of the cases, the model made robust using dual-perturbation attacks remains quite robust even as we evaluate against a different attack, using a different norm.

6. Conclusion

In this paper, we proposed the dual-perturbation attack, a novel threat model that produces *unsuspicious adversarial examples* by leveraging the cognitive distinction between image foreground and background. As we have shown, our attack can defeat all state-of-the-art defenses. By contrast, the proposed defense approaches using our attack model can significantly improve robustness against unsuspicious adversarial examples, with relatively small performance degradation on non-adversarial data. In addition, our defense approaches can achieve comparable to, or better robustness than the alternatives in the face of traditional attacks.

Our threat model and defense motivate several new research questions. The first is whether there are more effective methods to identify foreground of images. Second, we noted that our dual-perturbation attacks do at times increase background salience; are there methods for ensuring that this does not happen? Third, can we further improve robustness to dual-perturbation attacks? Finally, while we provide the first principled approach for quantifying suspiciousness, there may be effective alternative approaches for doing so.

References

- Arnab, A., Miksik, O., and Torr, P. H. On the robustness of semantic segmentation models to adversarial attacks. In *IEEE Conference on Computer Vision and Pattern Recognition*, pp. 888–897, 2018.
- Bhattad, A., Chong, M. J., Liang, K., Li, B., and Forsyth, D. Unrestricted adversarial examples via semantic manipulation. In *International Conference on Learning Representations*, 2020.
- Borji, A., Cheng, M.-M., Jiang, H., and Li, J. Salient object detection: A benchmark. *IEEE transactions on image processing*, 24(12):5706–5722, 2015.
- Brown, T. B., Carlini, N., Zhang, C., Olsson, C., Christiano, P., and Goodfellow, I. Unrestricted adversarial examples, 2018.
- Carlini, N. and Wagner, D. A. Towards evaluating the robustness of neural networks. *IEEE Symposium on Security and Privacy*, pp. 39–57, 2017.
- Coates, A., Ng, A., and Lee, H. An analysis of single-layer networks in unsupervised feature learning. In *Proceedings of the fourteenth international conference on artificial intelligence and statistics*, pp. 215–223, 2011.
- Cohen, J. M., Rosenfeld, E., and Kolter, J. Z. Certified adversarial robustness via randomized smoothing. In *International Conference on Machine Learning*, 2019.
- Deng, J., Dong, W., Socher, R., Li, L., Kai Li, and Li Fei-Fei. Imagenet: A large-scale hierarchical image database. In *2009 IEEE Conference on Computer Vision and Pattern Recognition*, pp. 248–255, June 2009. doi: 10.1109/CVPR.2009.5206848.
- Eykholt, K., Evtimov, I., Fernandes, E., Li, B., Rahmati, A., Xiao, C., Prakash, A., Kohno, T., and Song, D. X. Robust physical-world attacks on deep learning visual classification. *IEEE/CVF Conference on Computer Vision and Pattern Recognition*, pp. 1625–1634, 2018.
- Goodfellow, I., Shlens, J., and Szegedy, C. Explaining and harnessing adversarial examples. In *International Conference on Learning Representations*, 2015.
- He, K., Zhang, X., Ren, S., and Sun, J. Deep residual learning for image recognition. In *Proceedings of the IEEE conference on computer vision and pattern recognition*, pp. 770–778, 2016.
- He, S. and Pugeault, N. Salient region segmentation. *arXiv preprint arXiv:1803.05759*, 2018.
- Kingma, D. P. and Ba, J. Adam: A method for stochastic optimization. *arXiv preprint arXiv:1412.6980*, 2014.
- Kimmerer, M., Wallis, T. S. A., Gatys, L. A., and Bethge, M. Understanding low- and high-level contributions to fixation prediction. In *IEEE International Conference on Computer Vision*, 2017.
- Lecuyer, M., Atlidakis, V., Geambasu, R., Hsu, D., and Jana, S. Certified robustness to adversarial examples with differential privacy. In *IEEE Symposium on Security and Privacy*, 2019.
- Lin, T.-Y., Maire, M., Belongie, S., Hays, J., Perona, P., Ramanan, D., Dollár, P., and Zitnick, C. L. Microsoft coco: Common objects in context. In *European conference on computer vision*, pp. 740–755. Springer, 2014.
- Long, J., Shelhamer, E., and Darrell, T. Fully convolutional networks for semantic segmentation. In *Proceedings of the IEEE conference on computer vision and pattern recognition*, pp. 3431–3440, 2015.
- Madry, A., Makelov, A., Schmidt, L., Tsipras, D., and Vladu, A. Towards deep learning models resistant to adversarial attacks. In *International Conference on Learning Representations*, 2018.
- Mohapatra, J., Weng, T. W., Chen, P.-Y., Liu, S., and Daniel, L. Towards verifying robustness of neural networks against semantic perturbations. In *International Conference on Learning Representations*, 2020.
- Moosavi-Dezfooli, S.-M., Fawzi, A., and Frossard, P. Deepfool: a simple and accurate method to fool deep neural networks. In *Proceedings of the IEEE conference on computer vision and pattern recognition*, pp. 2574–2582, 2016.
- Papernot, N., McDaniel, P., Jha, S., Fredrikson, M., Celik, Z. B., and Swami, A. The limitations of deep learning in adversarial settings. In *2016 IEEE European Symposium on Security and Privacy (EuroS&P)*, pp. 372–387. IEEE, 2016a.
- Papernot, N., McDaniel, P., Wu, X., Jha, S., and Swami, A. Distillation as a defense to adversarial perturbations against deep neural networks. In *2016 IEEE Symposium on Security and Privacy (SP)*, pp. 582–597. IEEE, 2016b.
- Raghunathan, A., Steinhardt, J., and Liang, P. Certified defenses against adversarial examples. In *International Conference on Learning Representations*, 2018.
- Redmon, J. and Farhadi, A. Yolov3: An incremental improvement. *arXiv*, 2018.
- Sharif, M., Bhagavatula, S., Bauer, L., and Reiter, M. K. Accessorize to a crime: Real and stealthy attacks on state-of-the-art face recognition. In *ACM SIGSAC Conference on Computer and Communications Security*, pp. 1528–1540, 2016.

- Sharma, Y. and Chen, P.-Y. Attacking the madry defense model with l_1 -based adversarial examples. In *ICLR-18 Workshops*, 2018.
- Szegedy, C., Zaremba, W., Sutskever, I., Bruna, J., Erhan, D., Goodfellow, I., and Fergus, R. Intriguing properties of neural networks. In *International Conference on Learning Representations*, 2014.
- Treisman, A. M. and Gelade, G. A feature-integration theory of attention. *Cognitive psychology*, 12(1):97–136, 1980.
- Vaishnavi, P., Cong, T., Eykholt, K., Prakash, A., and Rahmati, A. Can attention masks improve adversarial robustness?, 2019.
- Wang, S., Chen, Y., Abdou, A., and Jana, S. Mixtrain: Scalable training of verifiably robust neural networks, 2018.
- Xie, C., Wang, J., Zhang, Z., Zhou, Y., Xie, L., and Yuille, A. Adversarial examples for semantic segmentation and object detection. In *Proceedings of the IEEE International Conference on Computer Vision*, pp. 1369–1378, 2017.

A. Datasets

A.1. Segment-6

Similar to Vaishnavi et al. (2019), our Segment-6 dataset is obtained by preprocessing the Microsoft COCO dataset (Lin et al., 2014) with the following steps: First, we make use of the semantic segmentation mask and bounding boxes of images in the COCO dataset to produce images, the associated masks, and labels such that each image contains one object of interest. This makes the dataset compatible with image classification tasks. Then, we crop and resize the images and their semantic segmentation masks to squared images with 32×32 pixels. The statistics of the Segment-6 dataset are displayed in Table 2.

Class	Number of samples	
	Training	Test
Train	3,000	200
Bird	3,000	200
Cat	3,000	200
Dog	3,000	200
Toilet	3,000	200
Clock	3,000	200
Total	18,000	1,200

Table 2. Number of samples in each class of the Segment-6 dataset.

A.2. STL-7

The statistics of the STL-7 dataset are displayed in Table 3.

Class	Number of samples	
	Training	Test
Airplane	136	50
Bird	165	70
Car	221	95
Cat	63	28
Dog	200	84
Horse	210	80
Truck	251	93
Total	1,246	500

Table 3. Number of samples in each class of the STL-7 dataset.

A.3. ImageNet-10

The labels and number of images per class in the ImageNet-10 dataset are listed in Table 4.

B. Implementations

We implemented all the attack model, as well as the defense approaches in PyTorch⁴, an open-source library for neural network learning. We used the ResNet34 model (He et al., 2016) and standard transfer learning, as the datasets employed in our experiments do not have a sufficient amount of data to achieve high accuracy. Specifically, we initialized the network with the model pre-trained on ImageNet, reset the final fully connected layer, and added a *normalization layer* in front of the ResNet34 model, which performs a channel-wise transformation of an input by subtracting (0.485, 0.456, 0.406) (the mean of ImageNet) and then being divided by (0.229, 0.224, 0.225) (the standard deviation of ImageNet);⁵ then, we train the

⁴Available at <https://pytorch.org/>.

⁵To fit the Segment-6 dataset which contains much smaller images compared to ImageNet, we also reset the first convolutional layer of the pre-trained ResNet34 model by reducing the kernel size from 7×7 to 3×3 , stride from 2 to 1, and pad from 3 to 1.

Class	Number of samples	
	Training	Test
Airplane	346	42
Car	353	35
Cat	239	26
Dog	304	35
Truck	283	33
Elephant	366	31
Zebra	444	42
Bus	318	35
Bear	291	28
Bicycle	383	37
Total	3,327	344

Table 4. Number of samples in each class of the ImageNet-10 dataset.

Attack	Parameter	Value	Note
ℓ_∞ PGD	ϵ	8/255 for training AT-PGD; [4, 8, 12, 16]/255 for testing	Maximum ℓ_∞ perturbation
	α	$\epsilon/4$	Stepsize of PGD
	K	7 for training AT-PGD; 20 for testing	Number of PGD steps
ℓ_∞ dual-perturbation	ϵ_F	8/255 for training AT-Dual and Mix-Dual; [4, 8, 12, 16]/255 for testing	Maximum ℓ_∞ perturbation in foreground
	ϵ_B	$\epsilon_F * 5$	Maximum ℓ_∞ perturbation in background
	α_F	$\epsilon_F/4$	Stepsize of the dual-perturbation in foreground
	α_B	$\epsilon_B/4$	Stepsize of the dual-perturbation in background
	K	7 for training AT-Dual and Mix-Dual; 20 for testing	Number of dual-perturbation steps

Table 5. Hyper-parameters of ℓ_∞ attacks.

neural networks as usual.

Unless otherwise specified, we used 60 epochs with training batch size 50 for ImageNet-10, and 128 for Segment-6 and STL-7. We used Adam Optimizer (Kingma & Ba, 2014) with initial learning rate of 10^{-4} for *Clean* and *RS*, and 10^{-3} for *AT-PGD*, *AT-Dual*, and *Mix-Dual* respectively. We dropped the learning rate by 0.1 every 20 epochs. We set β , the hyper-parameter of *Mix-Dual* to be 0.5 so as to balance training loss on both non-adversarial and adversarial data. We set $\sigma = 0.25, 0.5$, and 1 for *Randomized Smoothing (RS)*, each used $n = 100$ noise-corrupted copies for each test sample at prediction time. Due to space limitations, we only present results for *RS* with $\sigma = 0.5$ in the main body of the paper; the others are presented in Section D of the Appendix.

As mentioned above, we implemented *PGD* and *dual-perturbation* attacks, bounded by both ℓ_∞ and ℓ_2 norms, to evaluate robustness of a classification model, as well as to build robust classifiers. We used the semantic segmentation masks on the Segment-6 dataset and the bounding box masks on STL-7 and ImageNet-10. Note that when we evaluated robustness of *Randomized Smoothing (RS)*, we used the *Smoothed Classifier* as the target classifier instead of the *Base Classifier* (Cohen et al., 2019), as the former is the one used at prediction time. To do this, we made a small modification to the regular PGD attack model: the adversary aims to maximize the expected loss of the prediction on adversarial examples with random Gaussian noise, instead of adversarial examples solely.⁶ The corresponding formulation is shown as follows:

$$\max_{\delta \in \Delta(\epsilon)} \mathbb{E}_{\eta \sim \mathcal{N}(\mathbf{0}, \sigma^2 \mathbf{I})} [\mathcal{L}(h_{\theta}(\mathbf{x} + \delta + \eta), y)] \quad (14)$$

where $\eta \sim \mathcal{N}(\mathbf{0}, \sigma^2 \mathbf{I})$, σ is the standard deviation of Gaussian noise used by *RS* at training and prediction time. The above optimization problem can be solved by a similar approach to the regular PGD attack: the only difference is that at each iteration k of the attack, we draw N ($N = 10$ in our experiments) samples of noise, add these to the adversarial example

⁶Note that the Gaussian perturbations are only used to compute the loss of the prediction; the resulting adversarial examples do not have Gaussian perturbations.

Towards Robustness against Unsuspicious Adversarial Examples

Attack	Parameter	Value	Note
ℓ_2 PGD	ϵ	Segment-6: 0.5 for training AT-PGD, [0.25, 0.5, 0.75, 1.0] for testing; STL-7: 1.0 for training AT-PGD, [0.5, 1.0, 1.5, 2.0] for testing; ImageNet-10: 2.0 for training AT-PGD, [1.0, 2.0, 3.0, 4.0] for testing	Maximum ℓ_2 perturbation
	α	$\epsilon/40$	Stepsize of PGD
	K	50 for training AT-PGD; 100 for testing	Number of PGD steps
ℓ_2 dual-perturbation	ϵ_F	The same value as ϵ	Maximum ℓ_2 perturbation in foreground
	ϵ_B	$\epsilon_F * 5$ for Segment-6; $\epsilon_F * 15$ for STL-7 and ImageNet-10	Maximum ℓ_2 perturbation in background
	α_F	$\epsilon_F/40$	Stepsize of the dual-perturbation in foreground
	α_B	$\epsilon_B/40$	Stepsize of the dual-perturbation in background
	K	50 for training AT-Dual and Mix-Dual; 100 for testing	Number of dual-perturbation steps

Table 6. Hyper-parameters of ℓ_2 attacks.

obtained at the current iteration, then compute the average gradient as follows:

$$\delta^{(k+1)} = \mathcal{P}_\epsilon(\delta^{(k)} + \alpha \mathcal{G}(\frac{1}{N} \nabla_{\delta^{(k)}} \mathcal{L}(h_{\theta}(\mathbf{x} + \delta^{(k)} + \boldsymbol{\eta}), y)))$$

Similarly, we also refined the *dual-perturbation* attack model when it is applied to examine robustness of RS, described in Section 3.2 of the paper. We list key hyper-parameters of attacks in Table 5 and Table 6.

C. Experimental Results for ℓ_∞ Norm

C.1. Saliency Analysis of ℓ_∞ Dual-Perturbation Adversarial Examples

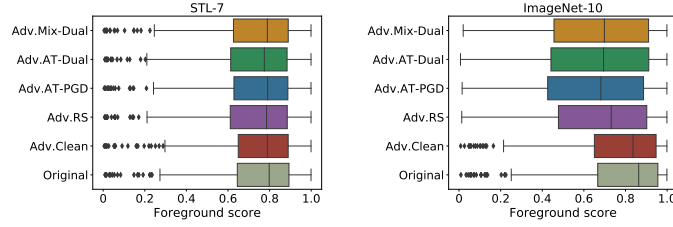


Figure 8. Saliency analysis: foreground score of the original and ℓ_∞ dual-perturbation examples in response to different defense approaches. AT-PGD, AT-Dual, and Mix-Dual are trained by using ℓ_∞ -norm attacks with hyper-parameters listed in Table 5. RS uses $\sigma = 0.5$. The ℓ_∞ dual-perturbation attack is performed with $\epsilon_F = 8/255$ and $\epsilon_B = 40/255$ Left: STL-7. Right: ImageNet-10.

Figure 8 presents the results of saliency analysis on the original and ℓ_∞ dual-perturbation examples. Similar to the results of the ℓ_2 -norm case presented in the main body of the paper, we can see that the *Foreground Score* tends to be above 0.7 for STL-7, and close to 0.7 for ImageNet-10. This indicates that predicted human fixation is relatively localized to the foreground. Moreover, we can see that the *Foreground Score* does not significantly decrease for dual-perturbation examples in response to robust classifiers (AT-PGD, RS, AT-Dual, and Mix-Dual), though we do note some tangible decrease in these examples on ImageNet-10. This indicates that it is more difficult to produce unsuspicious adversarial examples against robust models.

C.2. ℓ_∞ Dual-perturbation Attacks on Robust Classifiers

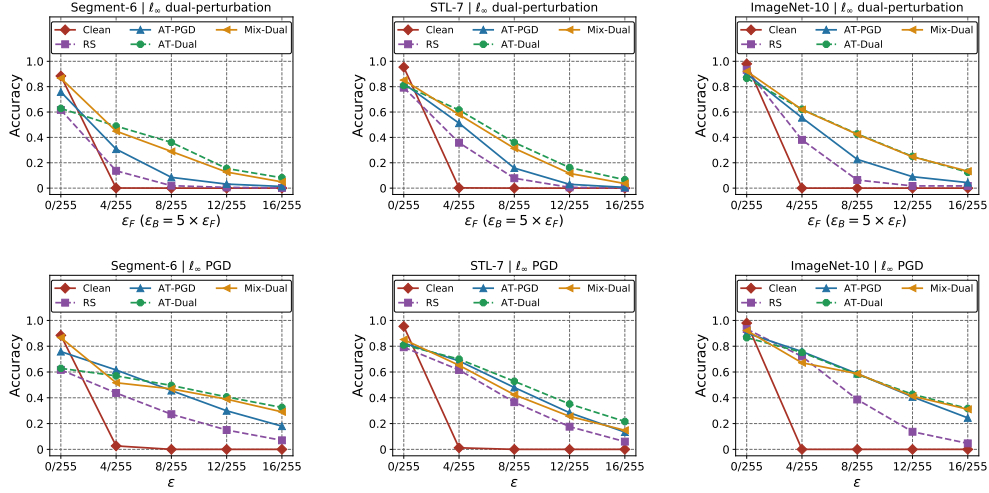


Figure 9. Robustness to white-box ℓ_∞ attacks with a variety of distortions on Segment-6 (left column), STL-7 (middle column), and ImageNet-10 (right column). AT-PGD, AT-Dual and Mix-Dual are trained by using ℓ_∞ -norm attacks with hyper-parameters listed in Table 5. RS uses $\sigma = 0.5$. Top: dual-perturbation attacks. Bottom: PGD.

Figure 9 presents robustness of classifiers (trained by using ℓ_∞ attacks) against white-box ℓ_∞ attacks. Our observations are similar to the case of ℓ_2 norms presented in Section 5 of the paper. First, our defense approaches, *AT-Dual* and *Mix-Dual*, remain significantly more robust to dual-perturbation attacks compared to the baselines. Second, all of the robust models remain robust to PGD attacks. A closer look at Figure 9 (bottom) shows that *AT-Dual* and *Mix-Dual* exhibit significantly more robustness than *RS* under PGD attacks with large distortions on Segment-6 and ImageNet-10 (e.g., when $\epsilon = 16/255$ on Segment-6).

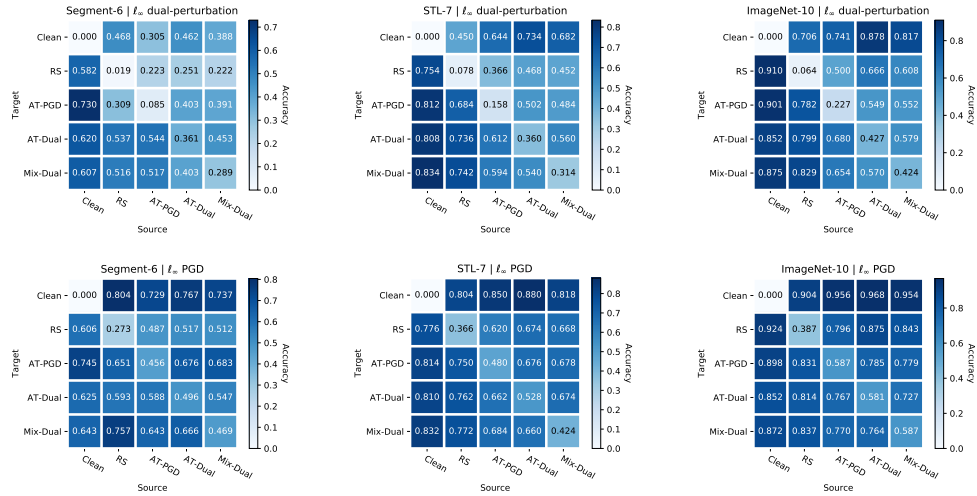


Figure 10. Transferability of adversarial examples on Segment-6 (left column), STL-7 (middle column), and ImageNet-10 (right column). AT-PGD, AT-Dual and Mix-Dual are trained by using corresponding ℓ_∞ -norm attacks with hyper-parameters listed in Table 5. RS uses $\sigma = 0.5$. Top: dual-perturbation attacks. Bottom: PGD.

Figure 10 presents the transferability of adversarial examples among different classification models. Again, we can observe that dual-perturbation attacks exhibit significantly better (up to 30%) transferability than the conventional PGD attacks. Moreover, *AT-Dual* and *Mix-Dual* are typically resistant to adversarial examples produced against other classifiers.

C.3. Generalizability of Defense

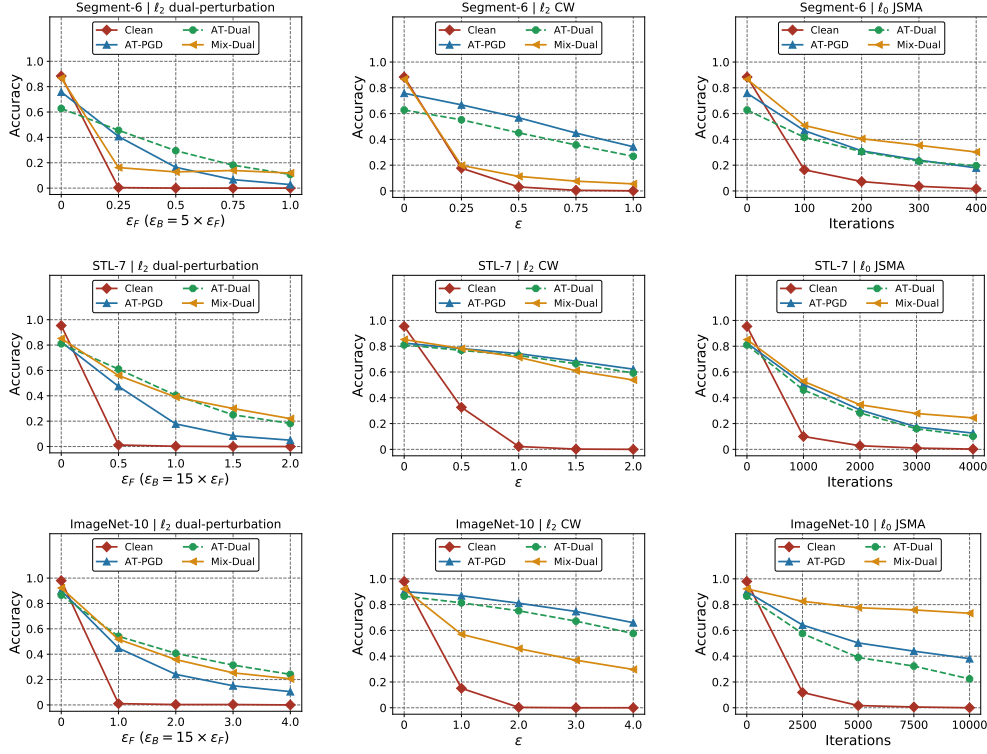


Figure 11. Robustness to additional white-box attacks on Segment-6 (top row), STL-7 (middle row), and ImageNet-10 (bottom row). AT-PGD, AT-Dual and Mix-Dual are trained by using corresponding ℓ_∞ -norm attacks with hyper-parameters listed in Table 5. Left: ℓ_2 dual-perturbation attacks. Middle: ℓ_2 CW attacks. Right: ℓ_0 JSMA attacks.

Figure 11 presents the adversarial robustness to additional white-box attacks. Here we evaluate models trained using ℓ_∞ -bounded attacks with the following alternative attacks: 1) dual-perturbation attacks with ℓ_2 -norm bounds (left column in Figure 11), 2) CW attacks using the ℓ_2 -bounded perturbations (middle column in Figure 11), and 3) JSMA attacks using the ℓ_0 norms (right column in Figure 11). Our first observation is that the proposed defense approaches, *AT-Dual* and *Mix-Dual* trained by using ℓ_∞ dual-perturbation attacks are significantly more robust to ℓ_2 -bounded dual perturbation attacks than *AT-PGD* trained by using ℓ_∞ -bounded PGD attacks. Our second observation is that the proposed *AT-Dual* method is comparable to *AT-PGD* in defending against CW and JSMA attacks, and the proposed *Mix-Dual* remains significantly more resistant to JSMA. However, we do note that using *Mix-Dual* can at times decrease the robustness to CW compared to the alternatives. For example, *Mix-Dual* is indeed fragile to CW attacks on Segment-6; on ImageNet-10, *Mix-Dual* is relatively robust to CW compared to the *Clean* model, but is still significantly less robust than *AT-PGD* and *AT-Dual*.

D. Supplemental Results for Randomized Smoothing

D.1. Variance in Gaussian Data Augmentation

Table 7, 8, 9, and 10 show the effectiveness of *Randomized Smoothing (RS)* against the proposed dual-perturbation attack. Here, we use different variances in Gaussian data augmentation of *RS*, and fix the number of noise-corrupted copies at prediction time, n to be 100. It can be seen that *RS* is generally fragile to the dual-perturbation attacks that are adapted to randomized classifiers. Moreover, increasing σ , the variance used in Gaussian data augmentation can only marginally improve adversarial robustness to dual-perturbation attacks while significantly decrease accuracy on non-adversarial data. However, we do observe that the improvement is considerably large (up to 20%) when we increase σ from 0.25 to 0.5 in the face of ℓ_2 dual-perturbation attacks on ImageNet-10.

Dataset	Defense approach	Attack Strength ($\epsilon_B = 5 \times \epsilon_F$)				
		$\epsilon_F = 0/255$	$\epsilon_F = 4/255$	$\epsilon_F = 8/255$	$\epsilon_F = 12/255$	$\epsilon_F = 1$
Segment-6	RS, $\sigma = 0.25$	71.4%	9.6%	0.4%	0.1%	0.0%
	RS, $\sigma = 0.5$	61.7%	13.7%	1.9%	0.6%	0.2%
	RS, $\sigma = 1$	47.7%	15.6%	2.8%	0.4%	0.2%
STL-7	RS, $\sigma = 0.25$	88.8%	27.8%	1.8%	0.2%	0.0%
	RS, $\sigma = 0.5$	79.2%	35.8%	7.8%	0.6%	0.2%
	RS, $\sigma = 1$	70.4%	34.4%	9.4%	1.4%	0.4%
ImageNet-10	RS, $\sigma = 0.25$	96.2%	18.9%	2.9%	1.2%	0.0%
	RS, $\sigma = 0.5$	93.3%	38.1%	6.4%	1.7%	1.7%
	RS, $\sigma = 1$	87.2%	37.5%	12.5%	4.1%	2.6%

Table 7. Robustness of *RS* against ℓ_∞ dual-perturbation attacks.

Defense approach	Attack Strength ($\epsilon_B = 5 \times \epsilon_F$)				
	$\epsilon_F = 0$	$\epsilon_F = 0.25$	$\epsilon_F = 0.5$	$\epsilon_F = 0.75$	$\epsilon_F = 1$
RS, $\sigma = 0.25$	71.4%	29.7%	6.7%	0.9%	0.1%
RS, $\sigma = 0.5$	61.7%	31.6%	11.8%	3.1%	1.3%
RS, $\sigma = 1$	47.7%	28.2%	14.4%	6.0%	1.5%

Table 8. Robustness of *RS* against ℓ_2 dual-perturbation attacks on Segment-6.

Defense approach	Attack Strength ($\epsilon_B = 15 \times \epsilon_F$)				
	$\epsilon_F = 0$	$\epsilon_F = 0.5$	$\epsilon_F = 1$	$\epsilon_F = 1.5$	$\epsilon_F = 2$
RS, $\sigma = 0.25$	88.8%	29.2%	5.8%	1.0%	0.4%
RS, $\sigma = 0.5$	79.2%	34.2%	10.4%	3.6%	1.2%
RS, $\sigma = 1$	70.4%	31.0%	11.8%	3.6%	2.0%

Table 9. Robustness of *RS* against ℓ_2 dual-perturbation attacks on STL-7.

Defense approach	Attack Strength ($\epsilon_B = 15 \times \epsilon_F$)				
	$\epsilon_F = 0$	$\epsilon_F = 1$	$\epsilon_F = 2$	$\epsilon_F = 3$	$\epsilon_F = 4$
RS, $\sigma = 0.25$	96.2%	18.0%	3.8%	2.6%	2.0%
RS, $\sigma = 0.5$	93.2%	34.6%	11.3%	3.8%	2.6%
RS, $\sigma = 1$	87.2%	38.4%	15.4%	8.1%	5.2%

Table 10. Robustness of *RS* against ℓ_2 dual-perturbation attacks on ImageNet-10.

D.2. Number of Samples with Gaussian Noise at Prediction Time

It has been observed that *Randomized Smoothing* (*RS*) can be computationally inefficient at prediction time as it uses a large number of noise-corrupted copies for each test sample at prediction time. It is natural to ask whether the prediction time of *RS* can be reduced without significantly sacrificing adversarial robustness in practice. We answer this question by studying the effectiveness of *RS* with different n , the numbers of noise-corrupted copies at prediction time. Specifically, we fix $\sigma = 0.5$ and set n to be 1, 25, and 100. Note that when $n = 1$, there is no two-sided hypothesis test for prediction; thus, no abstentions are obtained.

Here we use ℓ_∞ dual-perturbation attacks on *RS* for demonstration purposes. The results are shown in Table 11. It can be seen that when $n = 25$, the accuracy on both adversarial and non-adversarial data can drop by up to 10% compared to *RS* using $n = 100$. The reason is that under a small n , the prediction appears more likely to abstain. Interestingly, when $n = 1$, the accuracy can be marginally improved compared to $n = 100$, with the prediction time being reduced by 99%. This indicates that in practice, we would not lose accuracy without using the two-sided hypothesis test at prediction time.

Dataset	Defense approach	Attack Strength ($\epsilon_B = 5 \times \epsilon_F$)				
		$\epsilon_F = 0/255$	$\epsilon_F = 4/255$	$\epsilon_F = 8/255$	$\epsilon_F = 12/255$	$\epsilon_F = 1$
Segment-6	RS, $n = 1$	66.0%	19.8%	3.2%	0.8%	0.3%
	RS, $n = 25$	49.4%	9.1%	1.3%	0.5%	0.0%
	RS, $n = 100$	61.7%	13.7%	1.9%	0.6%	0.2%
STL-7	RS, $n = 1$	81.8%	44.2%	11.2%	1.6%	0.2%
	RS, $n = 25$	73.0%	29.0%	5.8%	0.4%	0.2%
	RS, $n = 100$	79.2%	35.8%	7.8%	0.6%	0.2%
ImageNet-10	RS, $n = 1$	93.9%	40.9%	7.6%	2.0%	1.7%
	RS, $n = 25$	89.8%	34.3%	5.5%	1.7%	1.7%
	RS, $n = 100$	93.3%	38.1%	6.4%	1.7%	1.7%

Table 11. Robustness of *RS* against ℓ_∞ dual-perturbation attacks under different numbers of noise-corrupted copies at prediction time.

E. Examples of Dual-Perturbation Attacks

E.1. ℓ_2 dual-perturbation examples on Segment-6

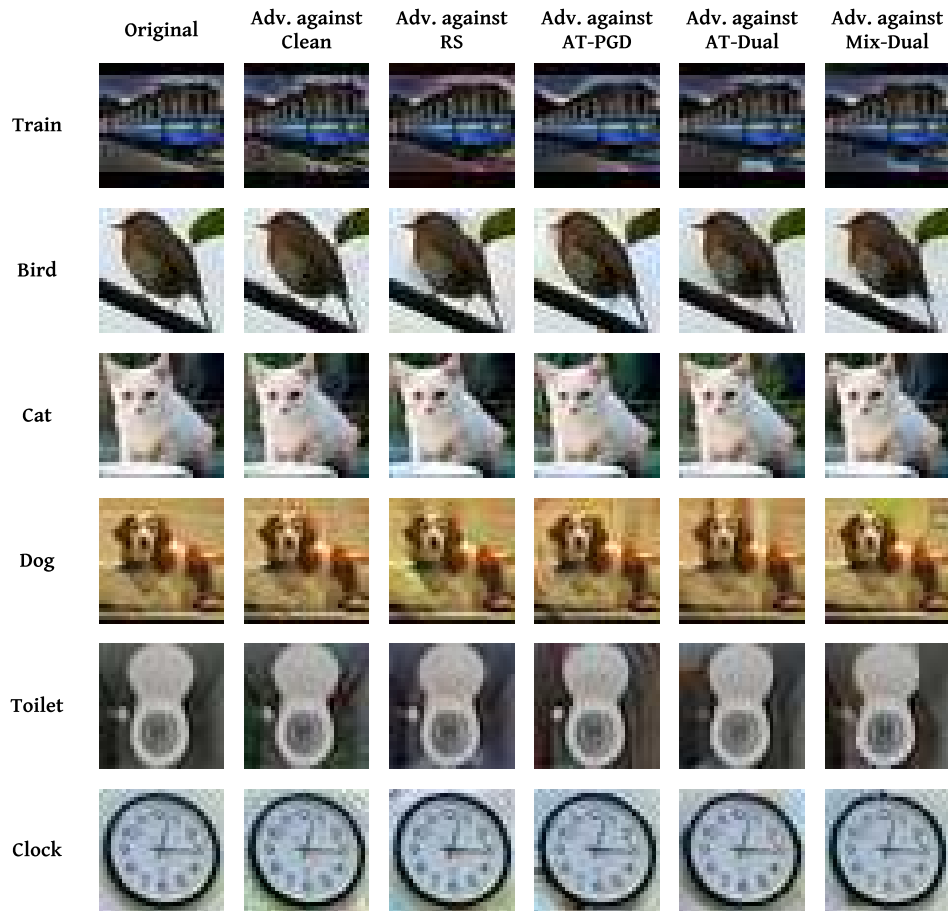


Figure 12. Segment-6: original examples and ℓ_2 dual-perturbation examples in response to different defense approaches. AT-PGD, AT-Dual and Mix-Dual are trained by using corresponding ℓ_2 -norm attacks with hyper-parameters listed in Table 6. RS uses $\sigma = 0.5$. Adversarial examples are produced by white-box ℓ_2 dual-perturbation attack ($\epsilon_F = 0.5$ and $\epsilon_B = 2.5$) against corresponding classifiers.

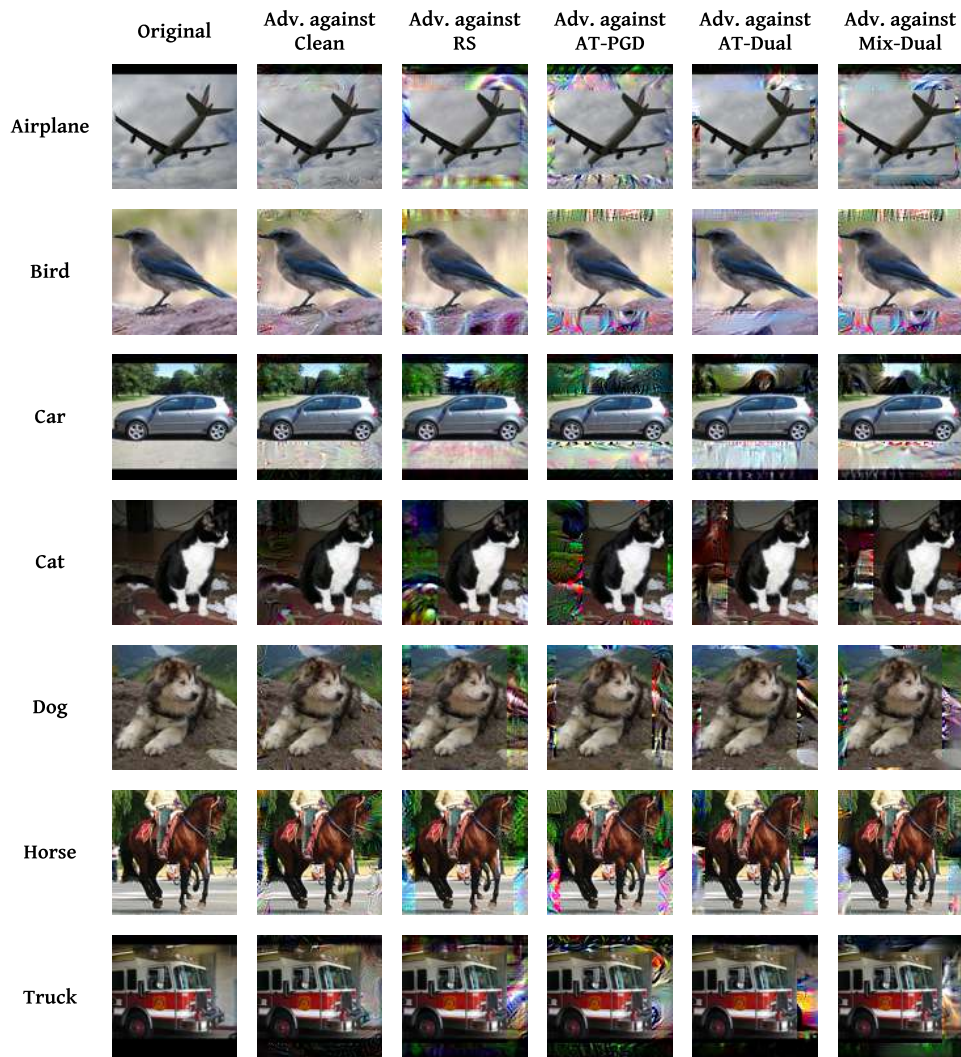
E.2. ℓ_2 dual-perturbation examples on STL-7

Figure 13. STL-7: original examples and ℓ_2 dual-perturbation examples in response to different defense approaches. AT-PGD, AT-Dual and Mix-Dual are trained by using corresponding ℓ_2 -norm attacks with hyper-parameters listed in Table 6. RS uses $\sigma = 0.5$. Adversarial examples are produced by white-box ℓ_2 dual-perturbation attack ($\epsilon_F = 1$ and $\epsilon_B = 15$) against corresponding classifiers.

E.3. ℓ_2 dual-perturbation examples on ImageNet-10

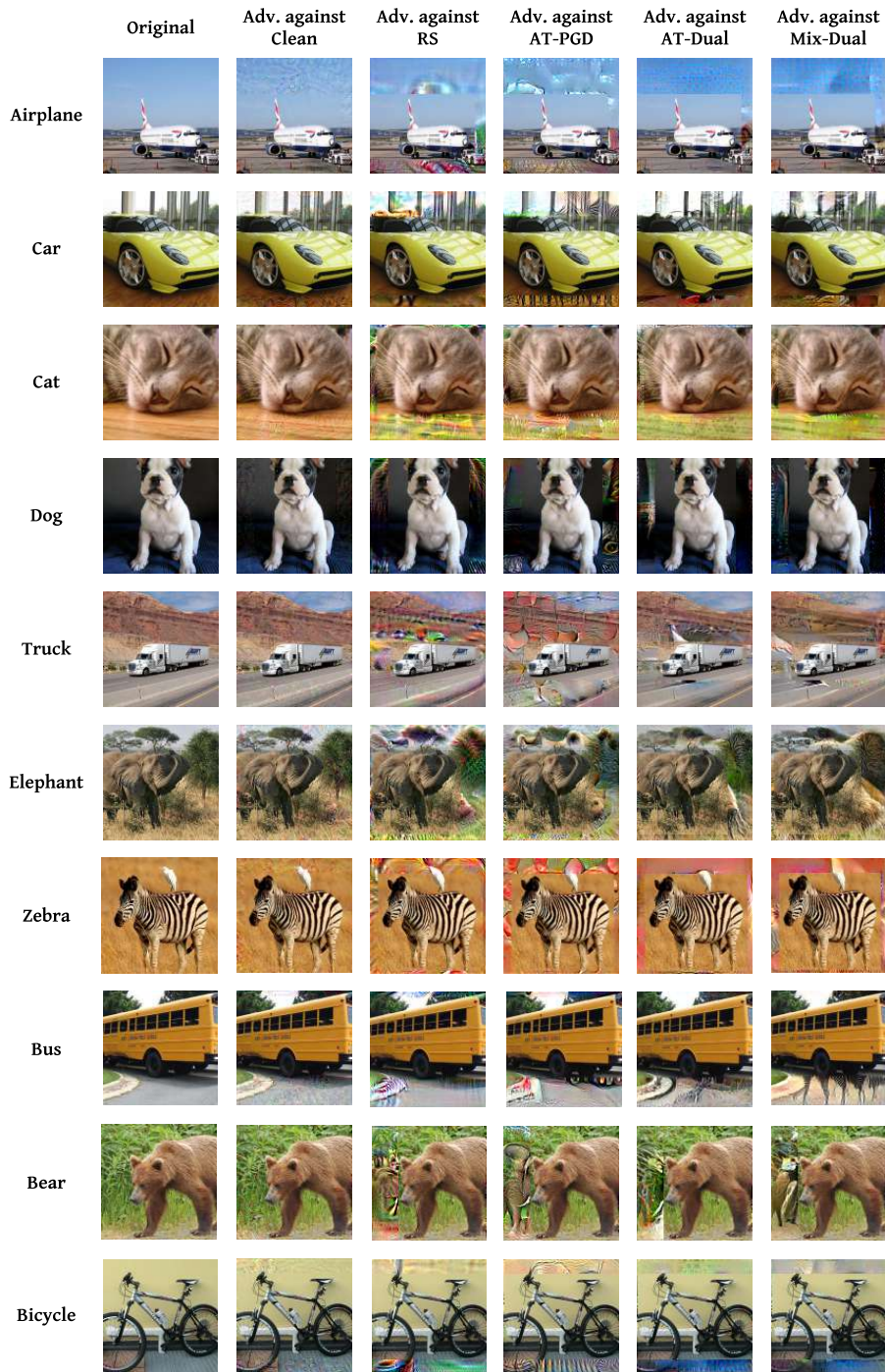


Figure 14. ImageNet-10: original examples and ℓ_2 dual-perturbation examples in response to different defense approaches. AT-PGD, AT-Dual and Mix-Dual are trained by using corresponding ℓ_2 -norm attacks with hyper-parameters listed in Table 6. RS uses $\sigma = 0.5$. Adversarial examples are produced by white-box ℓ_2 dual-perturbation attack ($\epsilon_F = 2$ and $\epsilon_B = 30$) against corresponding classifiers.

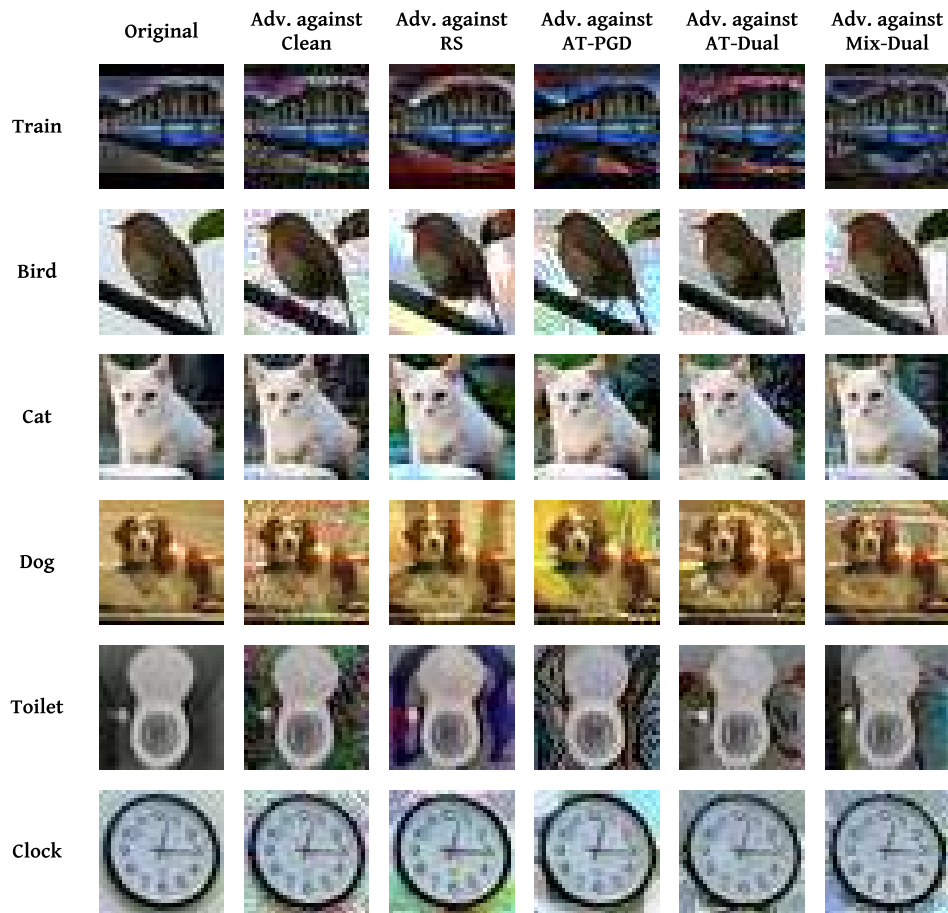
E.4. ℓ_∞ dual-perturbation examples on Segment-6

Figure 15. Segment-6: original examples and ℓ_∞ dual-perturbation examples in response to different defense approaches. AT-PGD, AT-Dual and Mix-Dual are trained by using corresponding ℓ_∞ -norm attacks with hyper-parameters listed in Table 5. RS uses $\sigma = 0.5$. Adversarial examples are produced by ℓ_∞ dual-perturbation attack ($\epsilon_F = 8/255$ and $\epsilon_B = 40/255$) against corresponding classifiers.

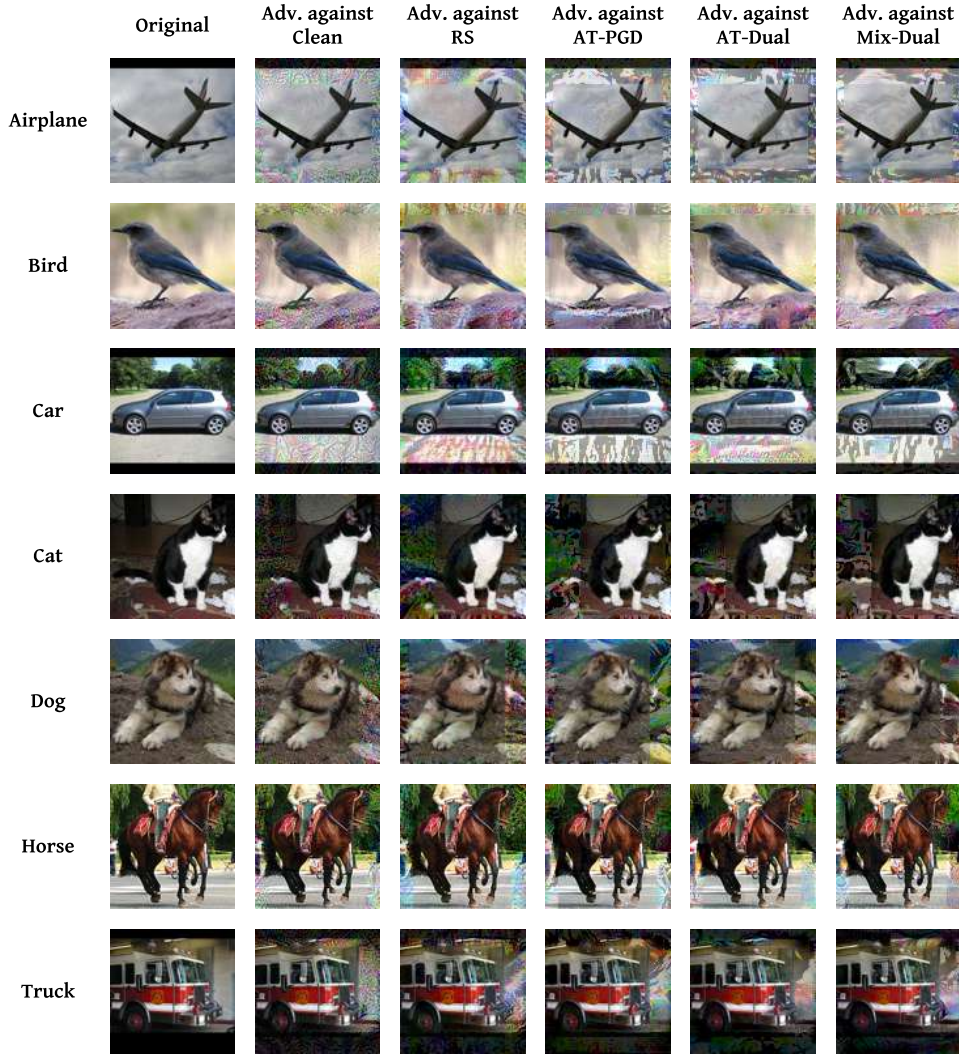
E.5. ℓ_∞ dual-perturbation examples on STL-7

Figure 16. STL-7: original examples and ℓ_∞ dual-perturbation examples in response to different defense approaches. AT-PGD, AT-Dual and Mix-Dual are trained by using corresponding ℓ_∞ -norm attacks with hyper-parameters listed in Table 5. RS uses $\sigma = 0.5$. Adversarial examples are produced by ℓ_∞ dual-perturbation attack ($\epsilon_F = 8/255$ and $\epsilon_B = 40/255$) against corresponding classifiers.

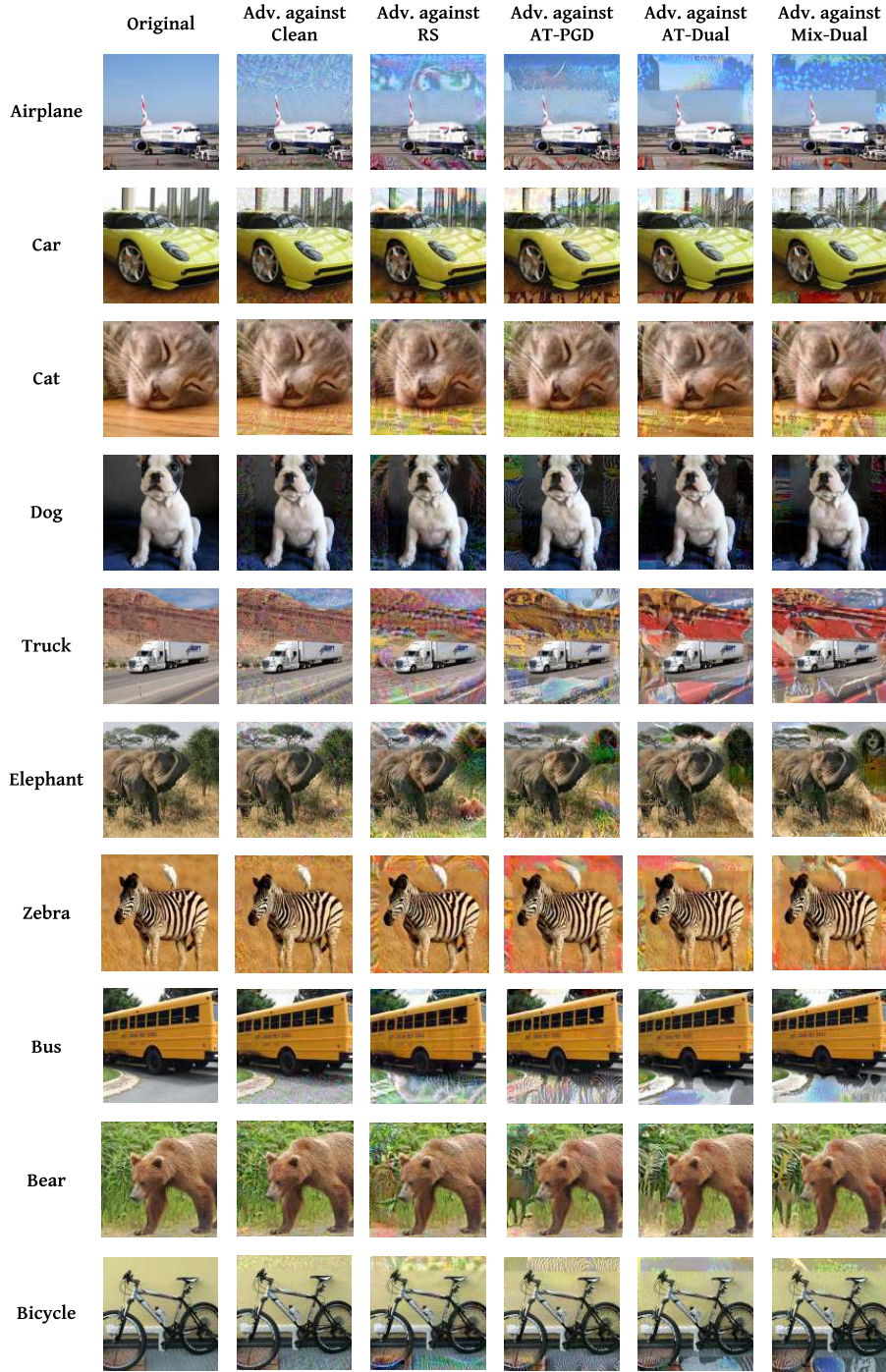
E.6. ℓ_∞ dual-perturbation examples on ImageNet-10


Figure 17. ImageNet-10: original examples and ℓ_∞ dual-perturbation examples in response to different defense approaches. AT-PGD, AT-Dual and Mix-Dual are trained by using corresponding ℓ_∞ -norm attacks with hyper-parameters listed in Table 5. RS uses $\sigma = 0.5$. Adversarial examples are produced by ℓ_∞ dual-perturbation attack ($\epsilon_F = 8/255$ and $\epsilon_B = 40/255$) against corresponding classifiers.